USGS
science for a changing world

Prepared for the National Aeronautics and Space Administration

Geologic Map of the Metis Mons Quadrangle (V–6), Venus

By James M. Dohm, Kenneth L. Tanaka, and James A. Skinner

Pamphlet to accompany
Scientific Investigations Map 3158

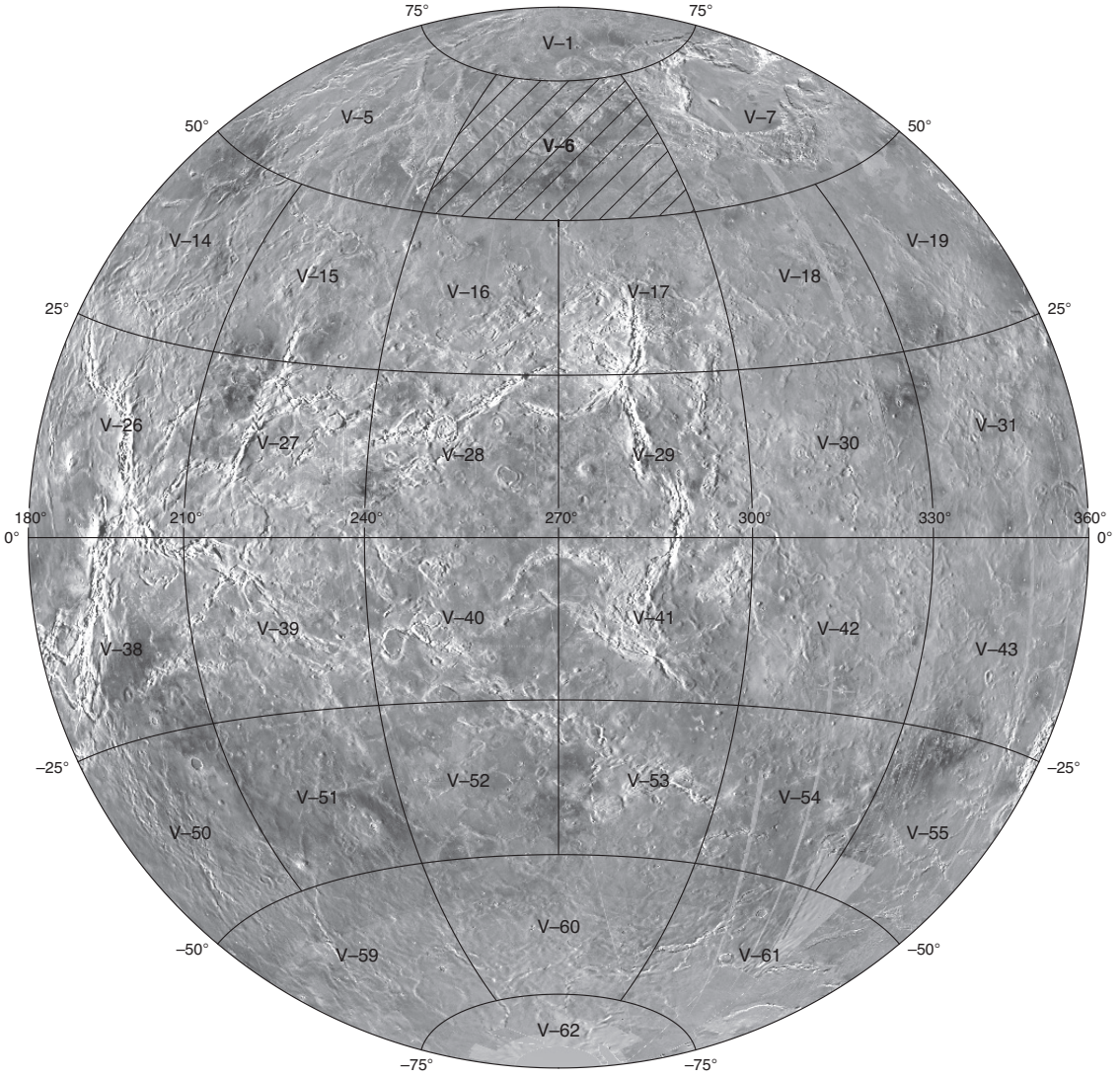

2011

U.S. Department of the Interior
U.S. Geological Survey

Contents

Tables

The Magellan Mission

The Magellan spacecraft orbited Venus from August 10, 1990, until it plunged into the Venusian atmosphere on October 12, 1994. Magellan Mission objectives included (1) improving the knowledge of the geological processes, surface properties, and geologic history of Venus by analysis of surface radar characteristics, topography, and morphology and (2) improving the knowledge of the geophysics of Venus by analysis of Venusian gravity.

The Magellan spacecraft carried a 12.6-cm radar system to map the surface of Venus. The transmitter and receiver systems were used to collect three data sets: (1) synthetic aperture radar (SAR) images of the surface, (2) passive microwave thermal emission observations, and (3) measurements of the backscattered power at small angles of incidence, which were processed to yield altimetric data. Radar imaging and altimetric and radiometric mapping of the Venusian surface were accomplished in mission cycles 1, 2, and 3 from September 1990 until September 1992. Ninety-eight percent of the surface was mapped with radar resolution on the order of 120 m. The SAR observations were projected to a 75-m nominal horizontal resolution, and these full-resolution data compose the image base used in geologic mapping. The primary polarization mode was horizontal-transmit, horizontal-receive (HH), but additional data for selected areas were collected for the vertical polarization sense. Incidence angles varied between about 20° and 45°.

High-resolution Doppler tracking of the spacecraft took place from September 1992 through October 1994 (mission cycles 4, 5, 6). Approximately 950 orbits of high-resolution gravity observations were obtained between September 1992 and May 1993 while Magellan was in an elliptical orbit with a periapsis near 175 km and an apoapsis near 8,000 km. An additional 1,500 orbits were obtained following orbit-circularization in mid-1993. These data exist as a 75° by 75° harmonic field.

Magellan Radar Data

Radar backscatter power is determined by (1) the morphology of the surface at a broad range of scales and (2) the intrinsic reflectivity, or dielectric constant, of the material. Topography at scales of several meters and larger can produce quasi-specular echoes, and the strength of the return is greatest when the local surface is perpendicular to the incident beam. This type of scattering is most important at very small angles of incidence, because natural surfaces generally have few large tilted facets at high angles. The exception is in areas of steep slopes, such as ridges or rift zones, where favorably tilted terrain can produce very bright signatures in the radar image. For most other areas, diffuse echoes from roughness at scales comparable to the radar wavelength are responsible for variations in the SAR return. In either case, the echo strength is also modulated by the reflectivity of the surface material. The density of the upper few wavelengths of the surface can have a significant effect. Low-density layers, such as crater ejecta or volcanic ash, can absorb the incident energy and produce a lower observed echo. On Venus, a rapid increase in reflectivity exists at a certain critical elevation above which high-dielectric minerals or coatings are thought to be present. This leads to very bright SAR echoes from virtually all areas above that critical elevation.

The measurements of passive thermal emission from Venus, though of much lower spatial resolution than the SAR data, are more sensitive to changes in the dielectric constant of the surface than to roughness. They can be used to augment studies of the surface and to discriminate between roughness and reflectivity effects. Observations of the near-nadir backscatter power, collected using a separate smaller antenna on the spacecraft, were modeled using the Hagfors expression for echoes from gently undulating surfaces to yield estimates of planetary radius, Fresnel reflectivity, and root-mean-square (rms) slope. The topographic data produced by this technique have horizontal footprint sizes of about 10 km near periapsis and a vertical resolution on the order of 100 m. The Fresnel reflectivity data provide a comparison to the emissivity maps, and the rms slope parameter is an indicator of the surface tilts, which contribute to the quasi-specular scattering component.

Introduction

The Metis Mons quadrangle (V–6) in the northern hemisphere of Venus (lat 50° to 75° N., long 240° to 300° E.; figs. 1*A* and 1*B*) includes a variety of coronae, large volcanoes, ridge and fracture (structure) belts, tesserae, impact craters, and other volcanic and structural features distributed within a plains setting, affording study of their detailed age relations and evolutionary development. Coronae in particular have magmatic, tectonic, and topographic signatures that indicate complex evolutionary histories (Barsukov and others, 1986; Basilevsky and others, 1986; Stofan and Head, 1990; Head and others, 1992; Janes and others, 1992; Sandwell and Schubert, 1992; Squyres and others, 1992; Stofan and others, 1992; Smrekar and Stofan, 1997; Chapman and Zimbelman, 1998).

Previously, the geology of the map region has been described either in general or narrowly focused investigations. Based on Venera radar mapping, a 1:15,000,000-scale geologic map of part of the northern hemisphere of Venus (Sukhanov and others, 1989) included the V–6 map region and identified larger features such as tesserae, smooth and hummocky plains materials, ridge belts, coronae, volcanoes, and impact craters but proposed little relative-age information. Global-scale mapping from Magellan data (Price and Suppe, 1994; Price and others, 1996) identified similar features and also determined their mean global ages with crater counts. However, the density of craters on Venus is too low for meaningful relative-age determinations at local to regional scales (Campbell, 1999). Several of the coronae in the map area have been described using Venera data (Stofan and Head, 1990), while Crumpler and others (1992) compiled detailed identification and description of volcanic and tectonic features from Magellan data.

The main purpose of this map is to reconstruct the geologic history of the Metis Mons quadrangle at a level of detail commensurate with a scale of 1:5,000,000 using Magellan data. We interpret four partly overlapping stages of geologic activity,

which collectively resulted in the formation of tesserae, coronae (oriented along structure belts), plains materials of varying ages, and four large volcanic constructs. Scattered impact craters, small shields and pancake-shaped domes, and isolated flows superpose the tectonically deformed materials and appear to be the most youthful materials in the map region.

Physiographic Setting

The Metis Mons quadrangle (V–6) is in the northern hemisphere of Venus and extends from lat 50° to 75° N. and from long 240° to 300° E. (fig. 1*A*). The quadrangle includes a backdrop of volcanic plains, mostly in the south half of the quadrangle (Kawelu, Libuše, and Guinevere Planitiae), whose mean elevation is within a few hundred meters of the mean planetary radius of 6,051.84 km (Ford and Pettengill, 1992) (fig. 2). Topographic highs are collectively produced by eight named ovoid tectonic centers known as coronae (from north to south: Bachue, Feronia, Otau, Azham, Coatlicue, Rananeida, Demeter, and Bau Coronae); two unnamed coronae features (one in the western plains and one forming an oblong ring in Mokosha Mons); four named broad volcanic shields (Metis, Bagbartu, Mokosha, and Atira Montes); one unnamed feature in east-central plains; and ridge and fracture belts (Ben, Okipeta, Varma-Ava, Chrykh-Keyok, Hemera, and Iyele Dorsa). These topographic highs range from hundreds of meters to >2.5 km in relief (tables 1 and 2; Stofan and Head, 1990) and extend >3.5 m above the mean planetary radius. Ridge and fracture belts generally define coronae boundaries, as well as systems of mostly aligned fractures (Ilbis and Minerva Fossae and Lampedo Linea), that extend for hundreds of kilometers. Outcrops of tessera material rise hundreds of meters above the low-lying plains in the northeast and southeast corners (Atropos and Senectus Tesserae, respectively) and along the west margin (Virilis Tesserae) of the map region. Small shield volcanoes, steep-sided domes (including Ale, Upunusa, and Nerthus Tholi), pitted cones, isolated lava flows, channel-form features (including Utrenitsa Vallis), and 21 impact craters (table 3) occur throughout the map area.

Data and Methodology

The Magellan mission to Venus acquired SAR backscatter, emissivity, reflectance, and topographic data for most of the planet. Image mosaics of radar backscatter (fig. 1*A*) were the primary data set used to delineate the boundaries of discrete geologic units and characterize their appearance, morphology, and distribution. Topographic data, rms slope, microwave emissivity, and corrected reflectivity data (figs. 2–5) provided insight into various physical properties of the surface. However, because the resolution of these datasets is relatively low (compared to the SAR base map) and the information conveyed therein is commonly influenced by surficial materials (rather than the regional geologic units), we used these data sets to help support more regional observations based on radar backscatter. We include basic radar statistics of the physical properties for each geologic unit (table 4). Derivations for radar backscatter (as outlined by Campbell, 1995) were not used to delineate the boundaries or contact relations of geologic units and are not included in table 4.

The discrete geologic units of the Metis Mons region were initially identified using photographic prints of ten full-resolution (75 m/pixel) Magellan SAR mosaics (F-MAPs) at 1:1,500,000 scale produced by the U.S. Geological Survey. Geologic contacts were hand-drawn on mylar overlays and then scanned, reprojected, vectorized, and merged within a geographic information system (GIS). All structure and surface features were digitally streamed into a dedicated GIS project using the digital Magellan backscatter base map. The spatial and interpretational accuracy of all scanned linework was iteratively quality checked and refined to produce an internally consistent 1:5,000,000-scale geologic map. The combined use of hand- and digital-mapping techniques resulted in increased spatial detail and accuracy of geologic information, as well as unit statistics (table 4) and area calculations (table 5). For clarity, all digitized unit outcrops that were <150 km^2 were individually analyzed and merged with adjacent units.

The remote, radar-based identification and interpretation of geologic materials, structures, and temporal relations for the production of a geologic map require a careful approach to avoid overinterpretation and maintain objectivity (for example, Wilhelms, 1972, 1990; Tanaka, 1994; Hansen, 2000). We delineated geologic units by coupling variation in the intensity of radar backscatter intensity with crosscutting relations among geologic units and surface features. However, some outcrops have insufficiently distinct stratigraphic, geomorphic, radar-backscatter, and (in some cases) tectonic character to merit a clear unit assignment. In these cases, we represent the unit and its boundary using the best lines of geologic and stratigraphic reasoning observed and appropriately convey the uncertainty in both the unit descriptions and map text.

Though radar data permit effective mapping of surface morphologies and structures (Daily and others, 1978; Ford and others, 1989, 1993; Sabins, 1997), geologic unit boundaries are often difficult to trace in comparison with those expressed by remote data sets typically available for rock surfaces on Earth and Mars. This is due to a limited radar-based perspective for Venus (with few look directions) versus a perspective gained through a greater diversity of data sets used in the remote geologic mapping of Earth and Mars (for example, visible and multi-spectral images, topography), which add greater perspective and thus greater confidence in differentiating rock material types, ages, and other fundamental characteristics and associations. In addition, even with distinctive features (for example, topographic promontories that are embayed by lava flows), there are wide-ranging confidence levels regarding where the position of the contact should be placed for parts of the outcrop margins. A particular challenge in radar-based geologic mapping is in the level of confidence attributed to identifying discrete volcanic flow units that are likely to consist of a range of surface roughnesses, which appear as grades of radar backscatter. Although stratigraphic clues such as structures may be helpful in delineating major stages in the emplacement of volcanic flows, they may be scattered and provide considerable local uncertainty in contact

placement. Because of these uncertainties, we use two different contact types. A certain contact is used where the unit margin is clearly demarcated. An approximate contact is used where the unit margin is unknown, gradational, or otherwise complex; in these instances, the contact may be drawn based on inferences made from the type and trend of local tectonic structures.

We attempted to determine ages of map units based on their emplacement relative to adjacent units (see table 5 and Correlation of Map Units). Thus, we avoid to the extent possible defining map units and basing unit ages on secondary structures that tend to obscure the origin and material age of the units (see Hansen, 2000). We recognize that the termination of tectonic structures and surface features likely represents either the actual extent of surface deformation or the margin of an onlapping unit where the structures are buried (Hansen, 2000). However, we are not able to wholly disregard the occurrence and continuity of tectonic structures and other surface features when defining geologic units and interpreting the geologic history. Some of the geologic units that we identify herein are delineated by the density and relative ages of structures that deform them. In some cases, burial by a younger unit is evidenced where multiple sets of structures disappear along a common boundary.

We have identified a total of 27 geologic units in the Metis Mons map region based on morphologic characteristics, geologic associations, and stratigraphic relations. These units can be subdivided into five major material groups: mons material, plains material, corona material, tessera material, and crater material. Because of the uncertainty in relative age among widely spaced outcrops of each unit, the upper and lower extents of the unit boxes are jagged in the Correlation of Map Units to depict those uncertainties. According to the format generally followed in planetary geologic maps (Tanaka, 1994), we arrange our groups and units in the Correlation of Map Units from youngest to oldest (left to right) and show crater materials at the far right.

Although many of the V–6 map units and structures are similar to those mapped in other Venus 1:5,000,000-scale quadrangles, we find that stratigraphic relations shown in table 5 are complex and only locally applicable. We therefore do not infer that our geologic reconstruction has relative-age significance and correlations with similar-appearing units and structures on regional to global scales as proposed by some (Grosfils and Head, 1994; Basilevsky and Head, 1995, 2000a; Ivanov and Head, 2001), and we acknowledge that more complex regional and global histories are possible (Guest and Stofan, 1999). The stratigraphy and locations of geologic contacts mapped in V–6 agree in some respects with those of the adjoining Pandrosos Dorsa (V–5) quadrangle (Rosenberg and McGill, 2001). This is most evident with tessera material, except where the V–5 map indicates “densely lineated terrain”. Our map differs moderately in the delineation and subdivision of plains materials due primarily to a differing approach to identifying map units.

Stratigraphy

In the following sections, we describe the map units generally from oldest to youngest and by unit groupings.

Tessera Material

Tessera material (unit t) is the oldest unit in the region, as documented elsewhere on Venus (Basilevsky and Head, 1995, 2000a; Tanaka and others, 1997; Ivanov and Head, 2001). However, tessera material outcrops are likely to consist of mixtures of materials and structures of varying ages and origins (Ivanov and Head, 1996; Gilmore and others, 1997, 1998; Hansen and others, 1997, 2000), including those resulting from large impacts into ancient, thin lithosphere (Hansen, 2006; Hansen and Young, 2007). Virilis and Atropos Tesserae occur in the southwestern and northeastern parts of the quadrangle, respectively, and are composed almost entirely of tessera material. Smaller and more discontinuous outcrops of tessera material occur in western Kawelu Planitia and eastern Libuše Planitia. Tessera material is defined by a high-backscatter surface and a minimum of two intersecting sets of tectonic structures, including lineaments and wrinkle ridges (Hansen and Willis, 1996, 1998). Tessera material within the map region commonly occurs as plateaus that are tens to hundreds of kilometers wide and that extend as much as 1 km above the surrounding plains (fig. 2). Structurally controlled depressions commonly appear to be occupied by plains-type materials of comparatively low backscatter (for example, lat 65.96° N., long –118.76° E.). The density and complex pattern of structures that characterizes tessera material within the map region imply that the unit resulted from multiple stages of deformation that obscure features associated with its primary emplacement. Tessera material is likely to form the basal geologic unit upon which all other geologic materials have been emplaced. Due to the structural complexity of tessera material and its defining nature to that unit, symbols depicted within the boundaries of the unit are intended to convey only the local type and trend of tectonic structures.

Corona Material

Following (and perhaps concurrent with) tessera formation, concentrated magmatic activity produced ten coronae (table 1) in the map region, partly made up of ten intensely or moderately deformed corona units: Otau Corona material (unit cO), Demeter Corona material (unit cD), Coatlicue Corona material (unit cC), older and younger Feronia Corona material (units cF_1 and cF_2, respectively), Rananeida Corona material (unit cR), Bau Corona material (unit cBu), Bachue Corona material (unit cBa), and older and younger Azham Corona (units cA_1 and cA_2, respectively). Coronae materials were mapped individually because they have spatially and geologically distinctive tectonic and magmatic histories (see Stofan and Head, 1990; Stofan and others 1992, 1997). Coronae materials generally make up the interiors and annuli of the coronae and adjacent plains made up of flows radiating outward from the annuli. In some cases, the coronae materials merge with plains units along approximate contacts. For the unnamed corona at lat 61° N., long 245° E., we identify part of its annulus as a topographic warp and part as unit p_2. It also has an interior depression that connects with a broad trough that extends northwest. However, we do not map a corona unit, because it appears largely indistinct with unit p_3 materials.

Timing relations among the coronae are largely uncertain. Only Feronia and Azham Coronae show distinct evidence for two stages of corona-related deformation; each corona is defined by two units of distinctly contrasting backscatter and structural characteristics. Feronia Corona contains material near its center that generally has low backscatter and few mappable lineaments relative to surrounding material. This material is mapped as younger Feronia Corona material (unit cF_2) and is interpreted to represent relatively less deformed, late-stage lava flows sourced from within Feronia Corona. Similarly, Azham Corona contains materials near its center and along its southern margin that generally have moderate backscatter and contrasting structural lineaments relative to its northern margin. This material is mapped as younger Azham Corona material (unit cA_2) and is interpreted to represent late-stage tectonism during corona growth.

Throughout the quadrangle, corona materials display high variability in their degrees of modificational states, generally ranging from Feronia Corona that displays a distinct, radar-bright annulus to Demeter Corona that displays an annulus subdued by inundation of lava plains, as indicated by the older parts that crop out through the plains. We identify a tectonic annulus 139 x 255 km across within Mokosha Mons as a corona-like feature made up of deformed plains units. The annulus rises as much as 300 m above the interior and may be the result of corona-like sagging due to loss of dynamic support (Herrick and others, 2005). Co-evolution of volcanic shield growth and corona-like activity is indicated by their temporal overlap, which has been documented for Atai Mons on Venus (Grindrod and others, 2006).

Plains Material

Plains materials (plains units p_1, p_2, p_3, and p_4) are interpreted to be lava plains and are divided according to four inferred stages of plains emplacement. The older units show significantly more deformation, as evidenced by their high backscatter and density of mappable structures, and have generally lost much of their planar character. The oldest of the plains materials, unit p_1, displays complex structure, including numerous wrinkle ridges and lineaments that are partly aligned with regional ridge and fracture belts and topographic warps. Unit p_1 is gradational and perhaps coeval with some older coronae materials, as well as some outcrops of tessera material, as evidenced by its high backscatter and structural complexity. For example, unit p_1 occurs as scattered, highly deformed outcrops west and south of Senectus Tessera in the southeastern part of the map. Unit p_2, however, appears to overlie unit p_1, infills low areas of Virilis Tessera, and is both similar in age to and younger than various adjacent corona material units (table 5). Material that has backscatter and structural characteristics of unit p_2 is in contact with unit t in Senectus Tessera. Structural features within unit p_2 likely record tectonic events associated with most of the same local and regional magmatic centers of activity that contributed to the deformation of unit p_1, but of generally lesser intensity and (or) longevity. Elongated patches of both units p_1 and p_2 have been deformed into ridge and fracture belts that are as much as 400 km long and several to tens of kilometers wide.

Subsequent to the emplacement and deformation of the older plains materials (units p_1 and p_2), widespread effusive volcanism erupted lavas that buried much of the older plains in the map region, resulting in unit p_3. This unit generally postdates units p_1 and p_2 and corona materials (see table 5) and is interpreted to have resulted from plains volcanism. However, the chief differentiating characteristics are significantly less associated wrinkle ridges and structural lineaments, which we interpret as having resulted from comparatively diminished tectonic activity. Sources for the eruption may be corona margins and (or) ancestral mons edifices located along ridge and fracture belts. Utrenitsa Vallis forms a system of sinuous, narrow (<1 to 3 km wide), singular or multiple channel forms within unit p_3 that extend hundreds of kilometers from near Montessori crater southward onto Guinevere Planitia and across topographic plains of very low relief, including between discontinuous ridge-forming outcrops of unit p_1. Locally, the channel system splays into braided reaches of multiple narrow channels, such as where it crosses the west terminus of Charykh-Keyok Dorsa. Overall, the channel fits the canali-type classification of Komatsu and others (1993); various modes of canali origin involving constructional and erosional processes and perhaps exotic lava compositions have been proposed (see Baker and others, 1997).

Emplacement of voluminous flood lavas from local sources such as fissures and central vents, which generally postdate the emplacement of unit p_3, resulted in small to moderately extensive outcrops in the low-lying regional plains, adjacent to some of the coronae and shield volcanoes, and within the floors of some of the larger impact craters. These materials mostly have variable backscatter, local structures, and small shields and are mapped as unit p_4. In places, unit p_4 is marked by narrow linear to anastomosing or intersecting networks of lineaments, narrow linear to anastomosing wrinkle ridges in parallel lines or intersecting networks, and volcanic edifices generally less than 5 km in diameter. Part of a large outcrop of unit p_4 east and south of Montessori crater may consist of microdunes superposed on units p_3 and p_4 (see next section and fig. 6). In addition, an outcrop of unit p_4 north of Atira Mons appears to be a landslide deposit originating from an east-facing amphitheater within an adjacent, steep-sided dome (mapped as unit pd). An unnamed channel-form feature occurs in unit p_4 north-northwest of Atira Mons. The channel form is 80 km long, trends east-west, and is <2 km wide for most of its length. The channel form is defined by a set of moderate backscatter surfaces that parallel a low-backscatter interior, suggesting a levee-bounded flow. Crosscutting relations with wrinkle ridges indicate that the channel-form feature predates and postdates local contractional ridge formation.

Plains dome material (unit pd) consists of five gently sloping to steep-sided edifices that protrude through or are emplaced onto adjacent plains and flow materials. The unit has an apparent stratigraphic position that correlates with the emplacement of units p_3 and p_4. The domes include circular, pancake-shaped features to irregular hills with scalloped margins that likely resulted from flank collapse (Guest and others, 1992). The domes may represent relatively viscous volcanism (McKenzie

and others, 1992) or growth of a lava dome beneath a solidified basaltic lava crust (Stofan and others, 2000).

Mons Material

Mons materials are predominantly defined by overlapping lobate margins and digitate terminations that are interpreted to be spatially and stratigraphically complex suites of lava flows sourced from multiple locations, including mons summit calderas and fractures. Volcanic eruptions that were generally centered along the axes and (or) intersections of major ridge and fracture belts and topographic warps resulted in the emplacement of complexly overlapping flows associated with the construction of large shield volcanoes known as Atira, Mokosha, Metis, and Bagbartu Montes (see table 2 for their dimensions). Their shield-forming lavas are grouped as mons materials. Each edifice consists of an older and younger unit that is separated by a time-transgressive contact. This inference is based on the occurrence of low-backscatter material generally located within the center of the mons edifices. Crosscutting relations between mons materials and surrounding plains show that the younger mons materials correlate with the youngest plains materials. These units generally abut and surround subtle topographic rises and ridge belts composed of older plains material (units p_1 and p_2), as well as adjacent corona materials.

Older Atira Mons material (unit mA_1) forms the bulk of the Atira Mons shield and includes flank flows that bury adjacent plains units p_3 and p_4, as well as linear and irregularly shaped outcrops of units p_2 and p_1. Well-defined lobes of unit mA_1 are apparent on the north and south flanks of Atira Mons and possibly reflect some of the later stages of volcanic eruption during the emplacement of the unit. The marginal flows abut and flow around topographic warps and collections of wrinkle ridges. The shallow summit caldera (~110 km in diameter) is higher on the west side and is filled with younger Atira Mons material (unit mA_2) that contains wrinkle ridges and several volcanic edifices of varying diameter. The summit caldera is broadly defined by a topographic warp. Compared to other mons features in the quadrangle, Atira Mons is the most symmetrical and has no distinct lineaments and few small volcanic edifices that might have served as source regions for the lavas of unit mA_1; such features might be buried. In addition, the flanks of Atira Mons are deformed by wrinkle ridges that generally parallel the orientation of those that occur in the surrounding, low-lying plains. This suggests that the latest growth of Atira Mons predates the contractional tectonism that deformed regional mons and plains materials.

Older Mokosha Mons material (unit mMo_1) consists of radiating flank and plains flows sourced from fractures and volcanic vent edifices within and peripheral to Mokosha Mons. Unit mMo_1 extends from the Mokosha Mons edifice to the northwest, where it abuts and flows around ridge and fracture belts comprised of unit p_1. Marginal flows extend across unit p_3 to the north, west, and south and unit p_4 to the east. The orientation of lobe margins mapped within unit mMo_1 implicates two possible regional vents for the unit. The main vent is likely the Mokosha Mons summit caldera, which is defined by a corona-like, deformed annulus ridge (made up of units p_1 and p_2). This annulus contains younger Mokosha Mons material (unit mMo_2), which is marked by multiple, small volcanic edifices. A secondary vent, also comprised of multiple volcanic edifices and fractures, is located on a moderate topographic rise to the northwest of the main Mokosha edifice (fig. 2). A younger mons material unit is not identifiable within or proximal to the secondary vent area.

Metis Mons forms the broadest and tallest volcano in the map region (table 2). Older Metis Mons material (unit mMe_1) generally lacks clear flow fronts and is exposed as patchy outcrops at the upper flanks and near the summit region of Metis Mons. Unit mMe_1 has moderate backscatter, likely due to the presence of lineaments. Though unit mMe_1 is interpreted to form the bulk of the shield, it is largely buried by the younger Metis Mons material (unit mMe_2), which consists of well-defined lobate flows with variable backscatter surfaces. The flows that compose unit mMe_2 radiate from Ilbis Fossae and extend in all directions, where they abut high-standing materials or terminate as digitate lobes in the plains. To the north, unit mMe_2 abuts and flows around the older and more heavily deformed Bachue Corona material (unit cBa). To the west, south, and east, unit mMe_2 abuts and flows around ridge-forming outcrops of units p_1 and p_2 and extends onto and buries low-standing occurrences of units p_3 and p_4. Unit mMe_2 is dissected by Ilbis Fossae, a major northwest-southeast-trending set of fractures. Numerous small volcanic shields along this axis likely formed in conjunction with the emplacement of the surrounding flow units.

Bagbartu Mons forms a major topographic high between Feronia and Coatlicue Coronae. Older Bagbartu Mons material (unit mB_1) is characterized by overlapping high- and low-backscatter lobes that are generally oriented radial to both a system of fractures on Feronia's southern rim and a summit caldera at the center of Bagbartu Mons. The unit extends to the east and west from the summit caldera for almost 600 km in each direction. Unit mB_1 abuts and flows around older plains and corona materials on the north and south flank. Backscatter markedly decreases at the base of the edifice where the unit extends across unit p_4 and is deformed by wrinkle ridges. Additionally, unit mB_1 appears to embay the west and north margins of Indira crater. Younger Bagbartu Mons material (unit mB_2) forms a field of relatively low backscatter plains within the summit caldera of Bagbartu Mons. Therein, the unit contains multiple small volcanic edifices and several structural lineaments, where it perhaps reflects late-stage growth of Bagbartu Mons. Summit lineaments may represent newly formed structures or the reactivation of ancient structures possibly predating the volcano's development and associated with a structure belt that may have linked Feronia and Coatlicue Coronae. Tectonism may have been related to the formation of the Bagbartu Mons summit caldera through evacuation of an underlying magma chamber.

In addition, we have mapped undifferentiated mons material (unit mu) in several locations throughout the quadrangle where the material consists of lobate margins but is not strictly associated with any major mons-forming edifice. The largest outcrop of this material defines the extent of a small unnamed mons located south of Bagbartu Mons and east of Coatlicue

Corona (lat 61.7° N., long 280.3° E.). This outcrop, which is on an east-west-trending topographic rise, has multiple small volcanic edifices and well-defined flow lobes that extend to the north onto unit p_4 and either abuts or grades into older Bagbartu Mons material (unit mB_1). To the south, unit mu extends over and perhaps grades with unit p_4, where it is deformed by a few fractures. Other isolated outcrops of unit mu include (1) northerly flows within unit p_4 north of (and perhaps sourced from) radial fractures of Feronia Corona, (2) westerly flows within unit p_3 west of Azham Corona, (3) northerly flows within unit p_4 north of Atira Mons, and (4) westerly flows within unit p_3 southeast of Otau Corona.

On Venus, large volcanoes may develop over sustained sites of mantle upwelling, facilitated by the absence of plate tectonics (McGovern and Solomon, 1998). According to McGill (1998, 2000), some shield volcanoes may evolve into coronae due to thinning of the lithosphere. In the V–6 quadrangle, we observe that Mokosha Mons includes coronae-like, extensional tectonic structures encircling the volcano's summit and embayed by shield lavas. Also, Metis Mons buries the southern part of the highly deformed structural ring of Bachue Corona; local fracturing of Ilbis Fossae indicates some minor, late-stage, corona-related deformation of the shield. Magmatic activity appears to have resulted in concentrated deformation, including possible reactivation of the pre-existing structural fabric at all four shield volcanoes, similar to the summit region of Bagbartu Mons. Thus large shields in the map region chiefly postdate the development of underlying and adjacent coronae. However, we recognize that key temporal relations between earlier development of the coronae and shields may be completely obscured.

Impact Crater Material

Among the youngest materials within the map region is crater material (unit c). The larger craters all appear to overlie surrounding units, except for Katya and Tolgonay craters that may be embayed by plains units p_3 and p_4, respectively. Crosscutting of crater materials by structures is generally difficult to determine using the Magellan radar backscatter data; four craters have ejecta that appear fractured, and two of those seem to have fractured rims. Crater material possesses distinctive hummocky textures, some of the highest backscatter of any map units in the map area, complex rims, and low- and high-backscatter haloes (see table 3 and next section) owing, in part, to cratering operating within the tremendously thick atmosphere (nearly 100 times that of Earth) and extreme surface temperatures of Venus (~750 K) (Campbell and others, 1992; Herrick and others, 1997; McKinnon and others, 1997). We recognize a possible deformed crater at lat 55.6° N., long 243.5° E. mapped as tessera material, which consists of radar-bright ridges and a subtle, central depression; however, it could also be a deformed volcanic vent. Some crater floors have high backscatter and appear to be relatively pristine, but others have low backscatter and may be flooded by younger lavas or impact melt and (or) are blanketed by aeolian deposits. Though the latter contain morphologies and backscatters most similar to unit p_4, stratigraphic associations that clearly differentiate unit p_4 from unit p_3 on the floors of craters are lacking. As a result, these localized plains-unit designations should be treated with appropriate uncertainty. Twelve craters <15 km in diameter were not mapped as unit outcrops but rather designated with map symbols. Craters >15 km in diameter, which typically occur as segmented and (or) embedded circular scarps, are identified with crater rim symbols. Though the west-facing, inner rim walls mostly appear steeper than other wall sections, this observation may result from the east-looking Magellan SAR observations for the map region. Altogether, 22 impact craters have been identified in V–6 (table 3).

Crater flow material (unit cf) commonly emanates from impact craters and displays mostly high-backscatter, coarse texture, and lobate margins. Crater flows have a range of morphologic expressions, generally grade into crater rim and ejecta materials, and are interpreted to be chiefly composed of ejected impact melt.

Tectonic Structures

Magellan-based oblique radar illumination produces strong signal returns and peaks that highlight relative topographic highs (ridge and fracture belts, wrinkle ridges, and flow margins) and lows (channel forms, depressions), depending on shape, size (vs. radar resolution), roughness, and orientation with respect to radar illumination direction and wavelength (Tanaka and others, 2010). Structural features of inferred tectonic origin mapped in V–6 include wrinkle ridges, lineaments (generally interpreted as narrow graben or fractures), ridge and fracture belts (generally >15 km wide), and major topographic warps. Because these features are much too dense to map completely at 1:5,000,000, only representative structures are mapped to portray their general spatial distributions and orientations. Areas of very high backscatter mostly reflect high structural density, which obscures the original backscatter character of many map surfaces (for example, tessera outcrops).

Wrinkle ridges form sinuous ridges mostly <1 km wide and tens to hundreds of kilometers in length. Individually, these features have low relief, though collectively they can form major physiographic and topographic features. Most are organized into sets that are evenly spaced a few tens of kilometers apart and are most clearly recognized on dark plains and coronae units. The more prominent ridge sets follow subparallel, gently curving trends; less prominent wrinkle ridges commonly are oriented orthogonally to the trend of prominent wrinkle ridges to form a localized reticulate pattern. Wrinkle ridges on Venus generally represent modest, distributed crustal shortening (<5%) in the brittle upper crust (Banerdt and others, 1997).

Lineaments are several to tens of kilometers long and generally 1 to 2 km wide and have radar-bright margins and darker floors, some of which may be flooded by younger lavas. However, most lineaments are too narrow to resolve their relief, but they are commonly aligned with wider ones that form linear troughs. Thus, we generally interpret these features to be narrow graben or fractures (Banerdt and others, 1997). In V–6, lineaments can form dense, anastomosing swarms (for example,

Minerva Fossae), sometimes accompanied by interspersed wrinkle ridges (for example, Lampedo Linea). Lineaments are common tectonic structures in tessera material (unit t) and in regions of more highly deformed coronae, plains, and mons materials. Lineaments are likely to result from shallow crustal extension and may radiate from major volcanic and tectonic features, which may be underlain by igneous dikes in cases (Grosfils and Head, 1994).

Ridge and fracture belts are linear to dense arcuate collections of ridges and fractures that are generally >15 km wide, 100 to 500 km long, and hundreds to more than a thousand meters high. They generally occur in swarms where a concentration of contractional strain has accumulated due to compressive stresses oriented normal to their origins, perhaps driven by stresses within the mantle (Banerdt and others, 1997, and references therein). Subsequent extension, perhaps as the result of magmatic-driven activity and (or) overthickening of the underlying crust, results in the formation of fractures. In most cases, ridge and fracture belts in V–6 form moderate topographic warps in older plains units, as well as in certain corona rims. In places, they are densely deformed by fractures, smaller wrinkle ridges, and lineaments, many of which are likely not detectable due to the high backscatter of these regions. Herein, we map the major trends and axes of these features.

Topographic warps are broad features that have variable width, length, and height. These are discriminated from ridge and fracture belts due to the fact that they are not always expressed by dense collections of ridges and fractures. Often, topographic warps can trend both parallel and perpendicular to wrinkle ridges and lineaments and define the annuli of some regional coronae (for example, Azham, Coatlicue, and Rananeida Coronae). Topographic warps characteristically define the ellipsoidal annulus of Demeter Corona within plains unit p3, as well as in the summit depressions of regional mons features.

Surficial Features

The map units and structure in the Metis Mons quadrangle show modest correlations with Magellan backscatter, altimetry, rms slope, emissivity, and reflectivity (figs. 1–5; table 4). Commonly, differences in radar backscatter are sufficiently distinct among adjacent map units and their structures to help delineate unit boundaries. The brightest units in radar backscatter have the coarsest texture at radar wavelength (12.6 cm) and (or) steep facets that produce mirror-like reflections of the radar signal. These include the densely fractured tessera material, plains unit p_1, and earlier coronae materials. Also, the mons flow units show relatively bright individual flow surfaces, notably for parts of the younger Bagbartu flow material. The bright flows may result from the rugged texture of aa lava (Plaut, 1991). Similarly, crater materials have high backscatter that likely represents rugged textures of coarse, rubbly ejecta and perhaps aa-like impact melt flows. On the other hand, older plains and flow units generally show less distinctive radar backscatter signatures probably owing to weathering and burial by aeolian fines that mute the surface textures. In places, relatively bright, diffuse splotches detected on plains appear to be wind streaks that may include dunes.

Emissivity, reflectivity, and rms-slope data, however, show substantially lower resolution than the Magellan SAR that was primarily used as the base map for geological mapping. In many instances, these data are likely to relate to surface properties rather than to bedrock geology. Emissivity and reflectivity data for Venus have spatial resolutions of ~30–70 km and mainly correspond to the small-scale surface roughness and density of surface material (Pettengill and others, 1992); however, the dynamic ranges of these data in V–6 are too low to discriminate much geologically (table 4). The rms slope relates to meter-scale roughness and thus correlates with the original roughness character of materials, subsequent deformation, and (or) smoothing or roughening due to weathering or surficial deposition. The rms-slope mapping of the planet was completed at 5 km/pixel resolution (Ford and Pettengill, 1992).

Radar properties of surfaces associated with Montessori and Cotton craters show some striking associated patterns that indicate surficial materials. First, the craters are surrounded by diffuse, low-backscatter, low-emissivity parabolic haloes best observed on smooth plains. The haloes extend more than 1,000 km west of the craters and darken about half of the quadrangle from the northeast to the southwest corners (fig. 1). More than 50 such parabolic haloes associated with larger impact craters across Venus reportedly mark the redistribution of ejecta fines by a westward wind flow (Campbell and others, 1992). Hayashi crater also is surrounded by dark plains that may be halo material associated with this crater and (or) the extended halo of Montessori. Smaller haloes are associated with Indira, Golubkina, and Olya craters; these may have produced lesser amounts of fines and (or) the fines have been weathered and (or) dispersed.

Montessori crater shows some particularly interesting radar features. In the backscatter data, a 48-km-diameter circular dark splotch occurs 70 km east of the center of Montessori. The splotch has a small, 1.6-km-diameter crater centered within it and appears to form a small topographic high (fig. 2); thus, it likely represents a circular volcanic shield with a summit vent crater. Montessori is surrounded by an inner, low-backscatter parabolic halo that in turn is partly surrounded by a splotchy intermediate-backscatter, parabolic halo that is 100–200 km wide and is mapped as plains unit p_5. Also, some striped, low- and high-backscatter streaks trend east-west within ~150 km of the crater; no obvious deflections of the streaks around topographic features are observed. The rms-slope data show that, near the crater, the low-backscatter halo has low meter-scale roughness, whereas the bright halo has high roughness. The low-rms-slope inner parabola forms a tail as much as 300 km wide that extends perhaps more than 1,300 km west, crossing some moderate topographic slopes and overprinting the otherwise moderately high rms northern slope of Mokosha Mons, as well as some local structures; it also appears to be restricted in extent from the north by some densely lineated plains and the Rananeida Corona annulus.

We interpret that the splotchy intermediate-backscatter halo may consist of microdunes that produce a rough surface at meter scales in the rms slope data and have sides that face west

near the incidence angle of the radar beam (~27–30°). Because only left-looking backscatter data are available for this area, supportive information on the origin of these features, such as a reduced backscatter return using right-look data, is not available. In comparison, proposed microdunes in the southern hemisphere on Venus that are based on contrasting backscatter patches between left- and right-looking data, occur in association with three parabolic crater haloes (Weitz and others, 1994; Greeley and others, 1997). Those authors estimated that microdunes detected by such means have wavelengths on the order of 10 to 30 cm based in part on laboratory simulations. The low-rms-slope, low-backscatter, inner parabola extending west of Montessori may consist of a sufficient thickness of fines to significantly lower the decimeter- and meter-scale roughness and, hence, lower the backscatter and rms slope of the surface. Similar, west-trending, low-rms-slope, inner parabolas surrounded by high-rms-slope outer parabolas coalesce and extend west of the closely spaced craters Guan Daosheng and Eudocia (both in the Barrymore quadrangle, V–59; see Ford and Pettengill, 1992, fig. 1), which also have proposed microdunes (Weitz and others, 1994). The demarcation between the inner and outer parabolas may represent both impact-induced activity (including both winds and material emplacement) and prevailing winds and consequent winnowing of sand-size particles to form the outer parabolas. Because the outer halo does not cover the dark shield, the shield either postdates the dune material or it created an obstacle to dune migration.

Geologic History

The history of geologic events in the Metis Mons quadrangle (V–6) is recorded by the distribution and ages of the mapped material and tectonic units and their modificational features, which include extensional and contractional structures. We unravel their relative ages based on standard crosscutting, overlap, and embayment relations (Wilhelms, 1972, 1990; Tanaka, 1994; Hansen, 2000). Though radar data permit effective mapping of surfaces and structures (Ford and others, 1989, 1993; Sabins, 1997; Tanaka and others, 2010), several factors could influence the radar signature, including radar shadow, foreshortening, and layover (for example, Ford and others, 1993), and thus radar interpretation needs to be separated from geologic interpretation to the extent possible (for example, Hansen and others, 1999, 2000). In addition, we recognize that timing relations among and within geologic units and sets of tectonic structures are likely complex. For lava units, individual flows may span a time range that is poorly constrained by mapping relations, especially for sequences of stacked flows (for example, Guest and Stofan, 1999). Similarly, unique and identifiable structures can laterally transition into multiple tectonic fabrics that collectively display single or multiple morphologies and orientations developed over multiple stages of activity related to episodic magmatism at coronae and large volcanoes; some of these may involve other pre-existing structure belts (Bleamaster and Hansen, 2005). Given such geologic complexities and the inability for the mapping to provide full time constraints on the formation of geologic units and structures, we provide a generalized reconstruction of the geologic history of the Metis Mons quadrangle.

Geologic mapping indicates overlapping stages of major geologic activity (each of indefinite duration) for the Metis Mons (V–6) quadrangle of Venus (see Correlation of Map units). These stages can be characterized by the following dominant materials, from oldest to youngest: (1) tessera material; (2) materials of coronae and corona-like features and older plains units; (3) younger plains material and steep-sided domes; and (4) mons materials making up the large volcanic shields, isolated patches of flows, and crater and crater flow materials. Given the uncertainties and complexities previously mentioned, these stages represent peak and (or) waning periods in the cumulative production of the dominant exposed materials and features specified for each stage; rates of activity are uncertain. Each of the stages following the formation of tessera material resulted in a significant preserved record of areal resurfacing. Tectonically, some parts of coronae and various structural belts may have been active for most of the recorded geologic record of the Metis Mons map region, though activity waned or became more localized over time. Impact craters generally appear to be undeformed or modestly deformed, indicating that much of the deformation in the quadrangle occurred in a relatively short period of time and (or) deformation and volcanic resurfacing was effective at destroying older craters. The following discussion summarizes the geologic activity for each of these stages, which are named for their predominant features.

Tessera stage

This evolutionary stage of units within the V–6 quadrangle chiefly includes the formation of tessera materials, though older corona and plains materials might temporally overlap. The oldest materials in the V–6 quadrangle consist of isolated patches of relatively high standing tessera material surrounded by various plains materials; in places, tessera material is transitional with older coronae and plains materials deformed by similar complex structure but may also include other ancient crustal materials. Tessera material records the earliest and perhaps the largest degree of structural deformation in the map region; various models have been proposed to account for the crustal deformation that it records (for example, Basilevsky and others, 1986; Bindschadler and Head, 1991; Solomon and others, 1992; Hansen and Willis, 1996, 1998; Ivanov and Head, 1996; Gilmore and others, 1997, 1998; Hansen and others, 2000). The complex structural history of tessera material in the Metis Mons region is difficult to unravel and may include regional and global strain and deformation from now-unrecognizable local centers of magmatic activity, including coronae and structure belts or perhaps large impacts (Hansen, 2006).

Corona stage

This evolutionary stage of units within the V–6 quadrangle chiefly includes the formation of corona materials, as well as older plains materials (units p_1 and p_2). Coronae in the V–6

quadrangle display tectonic, volcanic, and topographic signatures that indicate complex evolutionary histories (table 1). The most highly deformed, generally older parts of the coronae are defined by structural complexities. These include prominent, high-radar backscatter, structurally complex ridge belts that commonly define the coronae annuli, as well as high-standing coronae interiors that have dominantly radial or intersecting patterns of grabens and lineaments and minor formation of wrinkle ridges at the interior margins. Coronae are interpreted to have formed contemporaneously with local to regional outcrops of plains units p_1 and p_2, perhaps as the result of magma plumes and convection cells blistering the surface of the map region. Plains units p_1 and p_2 collectively form structural belts in places and considerable overlap with tessera material development is possible, as evidenced by lateral gradations and because only plains unit p_2 of all corona stage units clearly postdates tessera material. Coronae development included dense radial and concentric fracturing and faulting, ridge development, and volcanism, resulting in complexly deformed lava sequences (in some cases, very similar in appearance to some of the tessera outcrops). The structures marking most outcrops of corona stage materials are more than an order of magnitude denser than the structures that deform younger plains materials. Broader structural interactions occur among coronae, especially where individual coronae are linked by major ridge and fracture belts. A major coronae belt trending ~N. 70° W. extends for >1,700 km across the center of the quadrangle and links structures that dominate Coatlicue, Rananeida, and Azham Coronae, as well as Lampedo Linea. Demeter Corona and others display annuli subdued by the inundation of lavas, which is indicated by the older parts of the corona that crop out through the relatively young plains materials. The ridge and fracture belts may also mark reactivated, pre-existing zones of lithospheric weakness, perhaps related to a phase of tectonism prior to a proposed global volcanic resurfacing event (Strom and others, 1994). Coronae and ridge and fracture belts may have been active for most of the recorded geological history of the Metis Mons map region, though activity apparently waned and became more localized during the plains and mons stages. Coronae are interpreted to have formed mostly via plume-driven tectonism, resulting in multiple concentric ridges and both radial and concentric lineaments within coronae and the adjacent plains materials (see Stofan and others, 1992, for details on formational models of coronae).

Plains stage

This evolutionary stage of units within the V–6 quadrangle chiefly includes the widespread emplacement and deformation of plains unit p_3, the most extensive geologic unit within the quadrangle (see table 5). During this stage, unit p_3 partly buried and (or) embayed older, generally more highly deformed materials and structures including tessera material and inactive or less active coronae and structure belts. Locally intense extensional and contractional deformation, including ridge and fracture belt growth, diminished, except for localized reactivation of faults within structural belts due to global to local stresses related to the relaxation of crustal materials and (or) the resurgence of corona activity. Instead, plains-stage tectonic deformation was dominated by distributed contraction and extension in the brittle upper crust that formed systems of wrinkle ridges and fractures. Lineaments generally parallel the northwest-southeast or northeast-southwest trends of regional structural belts. Wrinkle ridges generally trend concentric or radial to nearby coronae or appear to be influenced by other structure systems. The distributions and orientations of these features indicate that coronae-related and other local to regional stresses continued, and some of these structures likely resulted from reactivation and upward propagation of buried structures.

Mons stage

This evolutionary stage of units within the V–6 quadrangle chiefly includes the voluminous fissure-fed eruptions and major central volcanism related to the four large shield volcanoes—Atira, Mokosha, Metis, and Bagbartu Montes—as well as plains unit p_4. Geologic mapping indicates more than one episode of volcanism for some of the large shields. Some investigators have noted that collectively the broad shield volcanoes have among the lowest crater densities of any features on Venus (Namiki and Solomon, 1994; Price and Suppe, 1994; Basilevsky and Head, 2000b), but the timing of initial shield volcanism is uncertain. In addition, the growth of the four large shield volcanoes in the quadrangle led to local deformation within these features, including some rift-like faulting through Metis Mons to form Ilbis Fossae and perhaps relatively pronounced wrinkle-ridge development in places on the plains units surrounding Atira, Mokosha, and Metis Montes. Local corona and corona-like deformation during this stage formed an elongate structural annulus in Mokosha Mons, the caldera-like, partly enclosed depression at the summit of Atira Mons, the ridged annulus of Demeter Corona, and the complex radiating lineaments in northern Bagbartu Mons. Other lineaments associated with young lavas of plains unit p_4 reflect local extension related to fissure volcanism. Many impact craters postdate the emplacement of other materials formed during this stage according to superposition of their ejecta, including the more diffuse radar dark and bright haloes surrounding some of them (see table 3). These haloes appear to be made up of fines that are susceptible to redistribution by aeolian activity (for example, fig. 6).

Summary

In summary, the overall geologic sequence in the V–6 quadrangle represents a lowlands style of resurfacing and tectonism that demonstrates broad magmatic and tectonic evolution recorded in tessera and plains materials, as well as local evolution of coronae and large shield volcanoes. However, extensive uncertainties, exceptions, and complexities exist in determining precisely the relative ages of materials and features in the quadrangle. Some of the more notable uncertainties include (1) duration of plains volcanism (for example, catastrophic vs. gradual resurfacing) and how it may have evolved in style (for example, such as the dominance of shield vs. fissure vent types),

and (2) relative ages among spatially disconnected features ranging from small volcanic edifices, impact craters, and local structure systems to more extensive coronae structures and large shield volcanoes. Thus, the general stages in evolution described in this quadrangle show similar trends locally, but the mapping does not constrain the synchronicity among these local sets of features and the evolutionary stages they display. Given the available constraints, the geologic evolution of V–6 may be consistent with either (1) models involving discrete stages of global tectonic and volcanic activity (Basilevsky and others, 1997; Basilevsky and Head, 2000a,b; Ivanov and Head, 2001) combined with stages of regional, coronae development (Stofan and Head, 1990) or (2) scenarios of significantly more nondirectional, time-transgressive, activity (Guest and Stofan, 1999; Hansen, 2000; Hansen and Young, 2007).

Acknowledgments

We are grateful to the many Venus geologic mappers that have presented useful results and views, including comments on this mapping effort, at the annual Planetary Geologic Mapper's meetings, Lunar and Planetary Science Conferences, and other professional meetings; many of their methods and insights have been incorporated into this map. We especially thank Trent Hare, Bonnie Redding, and Donna Galuszka of the U.S. Geological Survey for assistance with the digital scanning, editing, and conversion of hand-drawn linework into a Geographic Information Systems-ready format and with image processing of gridded Magellan data sets.

References Cited

Baker, V.R., Komatsu, Goro, Gulick, V.C., and Parker, T.J., 1997, Channels and valleys, *in* Bougher, S.W., Hunten, D.M., and Phillips, R.J., eds, Venus II: Tucson, University of Arizona Press, p. 757–793.

Banerdt, W.B., McGill, G.E., and Zuber, M.T., 1997, Plains tectonics on Venus, *in* Bougher, S.W., Hunten, D.M., and Phillips, R.J., eds, Venus II: Tucson, University of Arizona Press, p. 901–930.

Barsukov, V.L., Basilevsky, A.T., Burba, G.A., and 25 others, 1986, The geology and geomorphology of the Venus surface as revealed by the radar images obtained by Veneras 15 and 16: Journal of Geophysical Research, v. 91, no. B4, p. D378–D398.

Basilevesky, A.T., and Head, J.W., 1995, Global stratigraphy of Venus—Analysis of a random sample of thirty-six test areas: Earth, Moon, and Planets, v. 66, p. 285–336.

Basilevsky, A.T., and Head, J.W., 2000a, Geologic units on Venus—Evidence for their global correlation: Planetary and Space Science, v. 48, p. 75–111.

Basilevsky, A.T., and Head, J.W., III, 2000b, Rifts and large volcanoes on Venus—Global assessment of their age relations with regional plains: Journal of Geophysical Research, v. 105, p. 24,583–24,611.

Basilevsky, A.T., Head, J.W., Schaber, G.G., and Strom, R.G., 1997, The resurfacing history of Venus, *in* Bougher, S.W., Hunten, D.M., and Phillips, R.J., eds, Venus II: Tucson, University of Arizona Press, p. 1047–1084.

Basilevsky, A.T., Pronin, A.A., Kryuchkov, V.P., Sukhanov, A.L., and Markov, M.S., 1986, Styles of tectonic deformations on Venus—Analysis of Venera 15 and 16 data: Journal of Geophysical Research, v. 91, p. D399–D411.

Bindschadler, D.L., and Head, J.W., 1991, Tessera terrain, Venus—Characterization and models for origin and evolution: Journal of Geophysical Research, v. 96, p. 5889–5907.

Bleamaster, L.F., III, and Hansen, V.L., 2005, Geologic map of the Ovda Regio quadrangle (V–35), Venus: U.S. Geological Survey Geologic Investigations Series Map I–2808, scale 1:5,000,000.

Campbell, B.A., 1995, Use and presentation of Magellan quantitative data in Venus mapping: U.S. Geological Survey Open-File Report 95–519, 32 p.

Campbell, B.A., 1999, Surface formation rates and impact crater densities on Venus: Journal of Geophysical Research, v. 104, p. 21,951–21,955.

Campbell, D.B., Stacy, N.J.S., Newman, W.I., and 5 others, 1992, Magellan observations of extended impact crater related features on the surface of Venus: Journal of Geophysical Research, v. 97, p. 16,249–16,277.

Chapman, M.G., and Zimbelman, J.R., 1998, Corona associations and their implications for Venus: Icarus, v. 132, p. 344–361.

Crumpler, L.S., Aubele, J.C., Senske, D.A., and 3 others, 1992, Volcanoes and centers of volcanism on Venus, *in* Bougher, S.W., Hunten, D.M., and Phillips, R.J., eds, Venus II: Tucson, University of Arizona Press, p. 697–756.

Daily, M., Elachi, Charles, Farr, T.G., and Schaber, G.G., 1978, Discrimination of geologic units in Death Valley using dual frequency and polarization imaging radar data: Geophysical Research Letters, v. 5, p. 889–892.

Ford, J.P., Blom, R.G., Crisp, J.A., and 6 others, 1989, Space radar observations—A guide for Magellan radar-image analysis: Jet Propulsion Laboratory, Publication 89-41, 126 p.

Ford, J.P., Plaut, J.J., Weitz, C.M., and 5 others, 1993, Guide to Magellan Image Interpretation: Jet Propulsion Laboratory, Publication 93-24, 148 p.

Ford, P.G., and Pettengill, G.H., 1992, Venus topography and kilometer-scale slopes: Journal of Geophysical Research, v. 97, p. 13,103–13,114.

Gilmore, M.S., Collins, G.C., Ivanov, M.A., Marinangeli, Lucia, and Head, J.W., 1998, Style and sequence of extensional structures in tessera terrain, Venus: Journal of Geophysical Research, v. 103, p. 16,813–16,840.

Gilmore, M.S., Ivanov, M.A., Head, J.W., III, and Basilevsky, A.T., 1997, Duration of tessera deformation on Venus: Journal of Geophysical Research, v. 102, p. 13,357–13,368.

Greeley, Ronald, Bender, K.C., Saunders, R.S., Schubert, G.G., and Weitz, C.M., 1997, Aeolian processes and features on Venus, *in* Bougher, S.W., Hunten, D.M., and Phillips,

R.J., eds, Venus II: Tucson, University of Arizona Press, p. 547–589.
Grindrod, P.M., Stofan, E.R., Brian, A.W., and Guest, J.E., 2006, The geological evolution of Atai Mons, Venus—A volcano-corona 'hybrid': Journal of the Geological Society of London, v. 163, p. 265–275.
Grosfils, E.B., and Head, J.W., 1994, The global distribution of giant radiating dike swarms on Venus—Implications for the global stress state: Geophysical Research Letters, v. 21, p. 701–704.
Guest, J.E., Bulmer, M.H., Aubele, J.C., and 6 others, 1992, Small volcanic edifices and volcanism in the plains of Venus: Journal of Geophysical Research, v. 97, p. 15,949–15,966.
Guest, J.E., and Stofan, E.R., 1999, A new view of the stratigraphic history of Venus: Icarus, v. 139, p. 55–66.
Hansen, V.L., 2000, Geologic mapping of tectonic planets: Earth and Planetary Science Letters, v. 176, p. 527–542.
Hansen, V.L., 2006, Geologic constraints on crustal plateau surface histories, Venus—The lava pond and bolide impact hypothesis: Journal of Geophysical Research, v. 111, E11010, doi:10.1029/2006JE002714.
Hansen, V.L., Banks, B.K., and Ghent, R.R., 1999, Tessera terrain and crustal plateaus, Venus: Geology, v. 27, p. 1071–1074.
Hansen, V.L., Phillips, R.J., Willis, J.J., and Ghent, R.R., 2000, Structures in tessera terrain, Venus—Issues and answers: Journal of Geophysical Research, v. 105, p. 4135–4152.
Hansen, V.L., and Willis, J.J., 1996, Structural analysis of a sampling of tesserae—Implications for Venus geodynamics: Icarus, v. 123, p. 296–312.
Hansen, V.L., and Willis, J.J., 1998, Ribbon terrain formation, southwestern Fortuna Tessera, Venus—Implications for lithosphere evolution: Icarus, v. 132, p. 321–343.
Hansen, V.L., Willis, J.J., and Banerdt, W.B., 1997, Tectonic overview and synthesis, *in* Bougher, S.W., Hunten, D.M., and Phillips, R.J., eds, Venus II: Tucson, University of Arizona Press, p. 797–844.
Hansen, V.L., and Young, D.A., 2007, Venus's evolution—A synthesis: Geological Society of America Special Paper 419, p. 255–273.
Head, J.W., Crumpler, L.S., Aubele, J.C., Guest, J.E., and Saunders, R.S., 1992, Venus volcanism—Classification of volcanic features and structures, associations, and global distribution from Magellan data: Journal of Geophysical Research, v. 97, no. E8, p. 13,153–13,198.
Herrick, R.R., Dufek, Josef, and McGovern, P.J., 2005, Evolution of large shield volcanoes on Venus: Journal of Geophysical Research, v. 110, E01002, doi:10.1029/2004JE002283.
Herrick, R.R., Sharpton, V.L., Malin, M.C., Lyons, S.N., and Feely, Kimberley, 1997, Morphology and morphometry of impact craters, *in* Bougher, S.W., Hunten, D.M., and Phillips, R.J., eds, Venus II: Tucson, University of Arizona Press, p. 1015–1046.
Ivanov, M.A., and Head, J.W., 1996, Tessera terrain on Venus—A survey of the global distribution, characteristics, and relation to surrounding units from Magellan data: Journal of Geophysical Research, v. 101, p. 14,861–14,908.
Ivanov, M.A., and Head, J.W., 2001, Geology of Venus—Mapping of a global traverse at 30° N. latitude: Journal of Geophysical Research, v. 106, p. 17,515–17,566.
Janes, D.M., Squyres, S.M., Bindschadler, D.L., and 4 others, 1992, Geophysical models for the formation and evolution of coronae on Venus: Journal of Geophysical Research, v. 92, no. E10, p. 16,055–16,068.
Komatsu, Goro, Baker, V.R., Gulick, V.C., and Parker, T.J., 1993, Venusian channels and valleys—Distribution and volcanological implications: Icarus, v. 102, p. 1–25.
McGill, G.E., 1998, Central Eistla Regio—Origin and relative age of topographic rise: Journal of Geophysical Research, v. 103, no. E3, p. 5889–5896.
McGill, G.E., 2000, Geologic map of the Sappho Patera quadrangle (V–20), Venus: U.S. Geological Survey Geologic Investigations Series Map I–2637, scale 1:5,000,000.
McGovern, P.J., and Solomon, S.C., 1998, Growth of large volcanoes on Venus—Mechanical models and implications for structural evolution: Journal of Geophysical Research, v. 103, no. E5, p. 11,071–11,101.
McKenzie, D., Ford, P.G., Liu, Fang, and Pettengill, G.H., 1992, Pancakelike domes on Venus: Journal of Geophysical Research, v. 97, no. E10, p. 15,967–15,976.
McKinnon, W.B., Zahnle, K.J., Ivanov, B.A., and Melosh, H.J., 1997, Cratering on Venus—Models and observations, *in* Bougher, S.W., Hunten, D.M., and Phillips, R.J., eds, Venus II: Tucson, University of Arizona Press, p. 969–1014.
Namiki, Noriyuki, and Solomon, S.C., 1994, Impact crater densities on volcanoes and coronae on Venus—Implications for volcanic resurfacing: Science, v. 265, p. 929–933.
Pettengill, G.H., Ford, P.G., and Wilt, R.J., 1992, Venus surface radiothermal emission as observed by Magellan: Journal of Geophysical Research, v. 97, p. 13,091–13,102.
Plaut, J.J., 1991, Radar scattering as a source of geologic information on Venus and Earth: St. Louis, Mo., Washington University, Ph.D. dissertation, 342 p.
Price, M.H., and Suppe, John, 1994, Mean age of rifting and volcanism on Venus deduced from impact crater densities: Nature, v. 372, p. 756–759.
Price, M.H., Watson, Geoffrey, Suppe, John, and Brankman, Charles, 1996, Dating volcanism and rifting on Venus using impact crater densities: Journal of Geophysical Research, v. 101, p. 4657–4672.
Rosenberg, Elizabeth, and McGill, G.E., 2001, Geologic map of the Pandrosos Dorsa quadrangle (V–5), Venus: U.S. Geological Survey Geologic Investigations Series Map I–2721, scale 1:5,000,000.
Sabins, F.F., 1997, Remote Sensing—Principles and Interpretation (3rd ed.): New York, W.H. Freeman and Company, 498 p.
Sandwell, D.T., and Schubert, Gerald, 1992, Flexural ridges, trenches, and outer rises around coronae on Venus: Journal of Geophysical Research, v. 97, no. E10, p. 16,069–16,083.
Smrekar, S.E., and Stofan, E.R., 1997, Corona formation and heat loss on Venus by coupled upwelling and delamination: Science, v. 277, p. 1289–1294.

Solomon, S.C., Smrekar, S.E., Bindschadler, D.L., and 8 others, 1992, Venus tectonics—An overview of Magellan observations: Journal of Geophysical Research, v. 97, p. 13,199–13,255.

Squyres, S.W., Janes, D.M., Baer, Gidon, and 4 others, 1992, Morphology and evolution of coronae on Venus: Journal of Geophysical Research, v. 97, p. 13,611–13,634.

Stofan, E.R., Anderson, S.W., Crown, D.A., and Plaut, J.J., 2000, Emplacement and composition of steep-sided domes on Venus: Journal of Geophysical Research, v. 105, no. E11, p. 26,757–26,771.

Stofan, E.R., Hamilton, V.E., Janes, D.M., and Smrekar, S.E., 1997, Coronae on Venus—Morphology and origin, *in* Bougher, S.W., Hunten, D.M., and Phillips, R.J., eds, Venus II: Tucson, University of Arizona Press, p. 931–965.

Stofan, E.R., and Head, J.W., 1990, Coronae of Mnemosyne Regio—Morphology and origin: Icarus, v. 83, p. 216–243.

Stofan, E.R., Sharpton, V.L., Schubert, Gerald, and 4 others, 1992, Global distribution and characteristics of coronae and related features on Venus—Implications for origin and relation to mantle processes: Journal of Geophysical Research, v. 97, p. 13,347–13,378.

Strom, R.G., Schaber, G.G., and Dawson, D.D., 1994, The global resurfacing of Venus: Journal of Geophysical Research, v. 99, p. 10,899–10,926.

Sukhanov, A.L., Pronin, A.A., Burba, G.A., and 9 others, 1989, Geomorphic/geologic map of part of the northern hemisphere of Venus: U.S. Geological Survey Miscellaneous Investigations Series Map I–2059, scale 1:15,000,000.

Tanaka, K.L., comp. (and 11 other contributors), 1994, The Venus Geologic Mappers' Handbook: U.S. Geological Survey Open-File Report 94-438, 66 p.

Tanaka, K.L., Anderson, R.C., Dohm, J.M., and 5 others, 2010, Planetary structural mapping, *in* Watters, T.R., and Schultz, R.A., eds, Planetary Tectonics: Cambridge, Cambridge University Press, p. 351–396.

Tanaka, K.L., Senske, D.A., Price, M.H., and Kirk, R.L., 1997, Physiography, geomorphic/geologic mapping, and stratigraphy of Venus, *in* Bougher, S.W., Hunten, D.M., and Phillips, R.J., eds, Venus II: Tucson, University of Arizona Press, p. 667–694.

Weitz, C.M., Plaut, J.J., Greeley, Ronald, and Saunders, R.S., 1994, Dunes and microdunes on Venus—Why were so few found in the Magellan data?: Icarus, v. 112, p. 282–295.

Wilhelms, D.E., 1972, Geologic mapping of the second planet: U.S. Geological Survey Interagency Report, Astrogeology 55, 36 p.

Wilhelms, D.E., 1990, Geologic mapping, *in* Greeley, Ronald, and Batson, R.M., Planetary Mapping: New York, Cambridge University Press, p. 208–260.

Table 1. Location and description of coronae and corona-like features of the Metis Mons quadrangle (V–6), Venus.
[---, no data]

Feature	Lat (° N.)	Long (° E.)	Trend	Size range[1] (km)	Elevation range[2] (m)	Height (m)	Interior moat or depression depth (m)	Exterior moat depth (m)	Moat width[3] (km)
Azham Corona	66.4	252.9	N. 51° W.	194–352	261–1,391	1,130	302	418	30–40
Bachue Corona	73.3	261.4	N. 79° E.	408–614	286–3,298	3,012	---	---	---
Bau Corona	52.8	259.3	N. 89° W.	322–529	239–1,671	1,432	311	---	60
Coatlicue Corona	63.4	273.9	N. 79° W.	270–380	299–1,474	1,175	---	---	---
Demeter Corona	53.9	294.8	N. 69° E.	406–816	–126–731	8,57	---	641	40–130
Feronia Corona	68.0	281.7	N. 80° W.	533–704	262–1,243	9,81	---	---	---
Mokosha Mons	57.7	255.0	N. 11° E.	139–255	1164–2,293	1,129	<300	---	---
Otau Corona	67.8	298.7	N. 64° W.	119–177	287–1,345	1,058	---	---	---
Rananeida Corona	62.6	263.5	N. 59° W.	431–469	255–1,161	906	576	---	80
Unnamed corona	61.1	245.0	N. 75° E.	80–150	–33–724	757	<500	---	---

[1]Size defined by outer margin of topographic annulus, locally defined by bounding ridge belts where topography is subtle.
[2]Values of surrounding plains elevation and highest feature elevation relative to mean planetary radius (MPR).
[3]Moats discontinuous except for those of Demeter Corona.

Table 2. Location and description of large volcanoes of the Metis Mons quadrangle (V–6), Venus.

Volcano	Lat (° N.)	Long (° E.)	Width (km)	Elevation range (m)	Height (m)
Atira Mons	52.2	267.6	600	276–1,498	1,222
Bagbartu Mons	65.5	279.0	300–750	275–1,612	1,337
Metis Mons	70.9	251.8	750–800	286–2,827	2,541
Mokosha Mons	57.5	255.0	500	312–2,293[1]	1,981
Unnamed mons	61.7	280.3	260–174	223–1,612	1,389

[1]Includes corona-like annulus at summit.

Table 3. Location and description of impact craters (21) of the Metis Mons quadrangle (V–6), Venus.

Crater name	Latitude (deg N.)	Longitude (deg E.)	Diameter (km)	Comments
Cotton	70.8	300.2	48.1	Only west edge in map area; bright floor (off map); extensive dark parabolic halo
Duncan	68.1	291.7	40.3	Small flow extends 40 km west; smooth, dark floor
Golubkina	60.3	286.5	28.4	Part of floor smooth, dark; small, irregular, dark halo
Hayashi	53.8	243.9	41.0	Moderately bright flows extend north and east <90 km; relaxed rim, smooth, dark floor
Hull	59.4	263.6	47.3	Flows extend west and southeast <110 km; smooth, dark floor
Indira	64.1	289.8	16.6	Very bright flows extend 35 km south; rough floor; small, irregular, dark halo
Johnson	51.8	254.6	24.5	Ejecta possibly fractured; smooth, dark floor
Julie	50.9	242.6	13.2	Relaxed rim; rough floor
Katya	52.8	285.7	10.5	Partly embayed on southwest flank by plains unit 3 (p_3); rough floor
Margit	60.1	273.1	14.0	Possibly south-trending impact; rough floor; possible ejecta patch 50 km south (see fig. 6)
Montessori	59.4	280.0	42.4	Small flow extends 30 km west; smooth, bright floor; extensive dark parabolic halo; bright halo forms swath east and south of crater; distinctive low rms slope; diffuse low emissivity plains west of crater
Natalia	67.1	272.9	10.8	Dark flows extend west (mapped as plains unit p_4); rough floor
Obukhova	70.7	289.7	46.0	Ejecta and rim fractured on west side; channels cut southwestern and northeastern ejecta; smooth, dark floor
Olya	51.4	291.8	13.4	Irregular dark halo may be flows (not mapped)
Outi	61.7	267.7	10.4	Possibly fractured, including possible flows (not mapped)
Tolgonay	68.8	271.1	4.6	Possibly partly embayed ejecta; fractured rim, ejecta; dark floor
unnamed	51.2	251.8	1.4	Bright ejecta
unnamed	66.8	297.2	2.8	Small crater south of Otau Corona; bright, speckled ejecta
unamed “a”	52.5	298.8	3.0	Western crater of pair south of Demeter Corona; bright ejecta rays
unnamed “b”	52.5	298.9	3.2	Eastern crater of pair south of Demeter Corona; bright ejecta rays
Zdravka	65.1	299.0	12.5	Flows extend <50 km southwest and northeast

Table 4. Elevation, emissivity, reflectivity, and rms-slope data of map units in the Metis Mons quadrangle (V–6), Venus.

Unit label	Elevation (m) [mean (min, max)]	RMS slope[1] (°) [mean (min, max)]	Emissivity [mean (min, max)]	Reflectivity [mean (min, max)]
mB_2	724 (389, 1,225)	3.0 (1.4, 6.7)	0.869 (0.866, 0.874)	0.16 (0.11, 0.28)
mMe_2	1271 (–197, 2,899)	3.4 (0.6, 9.0)	0.870 (0.857, 0.896)	0.11 (0.03, 0.26)
mMo_2	1821 (1533, 2,186)	3.2 (1.4, 4.6)	0.860 (0.851, 0.876)	0.13 (0.07, 0.20)
mA_2	958 (530, 1,508)	2.8 (1.5, 5.4)	0.863 (0.854, 0.876)	0.13 (0.09, 0.17)
mu	430 (–19, 1,626)	3.5 (1.1, 9.1)	0.866 (0.845, 0.896)	0.13 (0.06, 0.27)
mB_1	592 (–219, 1,697)	2.7 (0.7, 8.0)	0.869 (0.844, 0.895)	0.12 (0.05, 0.26)
mMe_1	1932 (1194, 2,406)	5.1 (1.0, 9.1)	0.872 (0.864. 0.878)	0.13 (0.08, 0.25)
mMo_1	809 (235, 2,370)	2.8 (0.6, 6.9)	0.863 (0.842, 0.901)	0.13 (0.07, 0.22)
mA_1	433 (–44, 1,392)	3.1 (0.6, 7.6)	0.860 (0.834, 0.915)	0.13 (0.07, 0.18)
pd	404 (–42, 1,753)	3.1 (1.3, 5.9)	0.858 (0.845, 0.886)	0.13 (0.08, 0.19)
p4	330 (–575, 1,582)	2.5 (0.5, 9.9)	0.862 (0.828, 0.927)	0.13 (0.05, 0.34)
p3	171 (–1322, 2,482)	2.6 (0.5, 10.0)	0.870 (0.838, 0.926)	0.11 (0.04, 0.31)
p_2	472 (–1340, 2,582)	3.3 (0.6, 9.9)	0.872 (0.834, 0.916)	0.11 (0.04, 0.33)
p_1	299 (–875, 2,354)	3.4 (0.6, 10.1)	0.877 (0.840, 0.910)	0.10 (0.04, 0.33)
cA_2	463 (–204, 1,087)	4.5 (1.2, 9.0)	0.888 (0.875, 0.899)	0.10 (0.06, 0.23)
cF_2	823 (142, 1,160)	3.7 (2.1, 7.7)	0.889 (0.885, 0.899)	0.080 (0.05, 0.16)
cBa	849 (–316, 3,641)	4.2 (0.6, 8.4)	0.874 (0.861, 0.885)	0.08 (0.02, 0.22)
cBu	724 (129, 1,314)	3.3 (1.0, 7.1)	0.897 (0.872, 0.915)	0.09 (0.06, 0.14)
cR	269 (–375, 829)	3.6 (0.7, 10.2)	0.882 (0.860, 0.913)	0.09 (0.05, 0.20)
cC	790 (–141, 1,682)	4.7 (0.6, 10.3)	0.884 (0.859, 0.900)	0.12 (0.05, 0.32)
cD	–47 (–339, 573)	2.7 (1.2, 5.9)	0.885 (0.875, 0.896)	0.107 (0.070, 0.135)
cO	881 (440, 1,368)	4.5 (1.8, 9.6)	0.878 (0.863, 0.883)	0.116 (0.070, 0.240)
cA_1	789 (–40, 1,396)	4.6 (2.2, 9.0)	0.883 (0.878, 0.890)	0.108 (0.060, 0.235)
cF_1	677 (–935, 1,275)	4.4 (1.2, 8.9)	0.887 (0.860, 0.900)	0.088 (0.040, 0.180)
t	809 (–700, 2,880)	3.9 (0.8, 10.2)	0.881 (0.845, 0.920)	0.093 (0.045, 0.255)
c	427 (–969, 2,053)	2.4 (0.5, 6.8)	0.865 (0.834, 0.903)	0.116 (0.070, 0.190)
cf	366 (–175, 1,193)	2.4 (0.8, 6.5)	0.874 (0.844, 0.915)	0.112 (0.070, 0.175)

[1]Values were extracted for each geologic unit from gridded, interpolated datasets (3.2 km/pixel resolution).

Table 5. Description of geologic map units of the Metis Mons quadrangle (V–6), Venus, including relative-age relations with adjoining map units.

[<, younger than; ~, relative in age with; >, older than]

Unit label	Unit name	Area (10^3 km^2)	Relative age relations
		Mons Materials	
mB_2	Younger Bagbartu Mons material	9	< mB_1; ~ mB_1
mMe_2	Younger Metis Mons material	492	< mMe_1, p_1, p_2, p_3, p_4, cBa, cA_2; ~ p_4, mMe_1
mMo_2	Younger Mokosha Mons material	20	< p_1, p_2, p_3, mA_1; ~ pd; > pd
mA_2	Younger Atira Mons material	9	< mA_1; ~ mA_1
mu	Mons material, undivided	57	< p_1, p_2, p_3, p_4, cC; ~ mB_1, p_4; > p_4
mB_1	Older Bagbartu Mons material	279	< cF_1, cC, p_2, p_3, p_4; ~ p_4, mu; > mu, c, cf
mMe_1	Older Metis Mons material	14	> mMe_2
mMo_1	Older Mokosha Mons material	276	< p_1, p_2, p_3; ~ mMo_2, p_4; > mMo_2, pd, p_4
mA_1	Older Atira Mons material	208	< p_1, p_2, p_3; ~ mA_2, p_4; > mA_2, p_4
		Plains Materials	
pd	Plains dome material	6	< mMo_1, mMo_2, p_1, p_3, p_4; ~ mMo_2, p_3
p_4	Plains unit 4	1.409	< mA_1, p_1, p_2, p_3, cBa, cBu, cR, cF_1, cO, t; ~ mMe_2, mu, mB_1, mA_1, c, cf; > mMe_2, mB_1, mu, pd, c, cf
p_3	Plains unit 3	2.993	< p_1, p_2, cA_1, cA_2, cBa, cBu, cR, cF_1, cC, cD, cO, t; ~ pd, c, cf; > mB_2, mMe_2, mMo_1, mA_1, pd, p_4, mu, c, cf
p_2	Plains unit 2	869	< p_1; mMe_1, cA_1, cBa, cR, cF_1, cC, t; ~ cR, cA_2, cC, cD, cO; > mB_1, mMe_2, mMo_1, mMo_2, mA_1, mu, p_3, p_4
p_1	Plains unit 1	383	< t; ~ cC, cR, cF_1, t; > mMe_2, mMo_1, mMo_2, mA_1, p_2, p_3, p_4, c, cf
		Corona Materials	
cA_2	Younger Azham Corona material	33	< cA_1; ~ p_2; > p_3, p_4, mMe_2
cF_2	Younger Feronia Corona material	10	< cF_1
cBa	Bachue Corona material	55	> p_2, p_3, p_4, mMe_2
cBu	Bau Corona material	18	> p_3, p_4
cR	Rananeida Corona material	34	~ p_1, p_2; > p_2, p_3, p_4
cC	Coatlicue Corona material	52	~ p_1, p_2; > p_2, p_3, p_4, mB_1, mu
cD	Demeter Corona material	8	~ cD; > p_3, p_4
cO	Otau Corona material	12	~ p_2; > p_3, p_4
cA_1	Older Azham Corona material	12	> p_2, p_3
cF_1	Older Feronia Corona material	136	~ p_1; > mB_1, mu, p_2, p_3, p_4, cF_2
		Tessera Material	
t	Tessera material	33	~ p_1; > p_1, p_2, p_3, p_4
		Crater Materials	
c	Crater material	40	< mB_1, p_1, p_3, p_4; ~ p_3, p_4
cf	Crater flow material	21	< mB_1, p_1, p_3, p_4; ~ p_3, p_4